Fig. 4. Dispersion data for the sample containing both donors and acceptors with structure Alq₃:PMMA|60 nm Ag|R6G:PMMA deposited onto a corrugated substrate. Data were obtained by recording the transverse-magnetic polarized (**A**) transmittance and (**B**) PL emission as a function of the in-plane wave vector of light, $k_x/2\pi$. Both are plotted with a logarithmic gray scale, where for (A), transmittance ranges from $T = 0.001$ (black) to $T = 0.1$ (white), whereas for (B), white represents minimum and black maximum PL emission. In each case, the data are dominated by the scattered features corresponding to the excitation and emission of both symmetric and antisymmetric coupled SPPs.

could act to channel energy from absorbing species to reaction centers and more generally in photochemistry near surfaces.

donor molecules on the far side of the silver film, whereas above $\lambda = 550$ nm there are two components to consider. In addition to the strong coupled SPP reradiation, which now arises from SPPs generated by the relaxation of acceptor molecules on the near side of the silver film (primarily excited by energy transferred from the donors), there is a broad emission band from $\lambda = 550$ to 675 nm, peaking at ~565 nm, which does not disperse with angle. This band is an order of magnitude more intense than for the acceptor-only sample (27) and corresponds to the enhanced acceptor emission previously seen in Fig. 2. This emission is direct radiation from acceptor molecules rather than grating-scattered reradiation from acceptor-excited SPP modes. Figure 4B clearly shows that both donors and acceptors strongly excite the coupled SPP

modes of the structure, that strong acceptor emission arises from excitation of the remote donor layer, and that the total emission from the structure can be strongly enhanced by recovering coupled SPP emission from both donor and acceptor through scattering from the grating microstructure.

A direct application of the strategy outlined above would be to top-emitting organic light-emitting diodes. Such devices are attractive for display applications where emission occurs through a metallic cathode. We have shown that depositing a dielectric layer on the surface of the device may lead to greater efficiency (7), and by dye-doping this layer SPP-mediated energy transfer could increase the spectral coverage of the output. Another potential area of application is synthetic light harvesting structures; SPP modes

References and Notes
1. H. X. Xu, E. J. Bjerneld, M. Kall, L. Borjesson, *Phys. Rev. Lett.* **83**, 4357 (1999).
2. S. M. Nie, S. R. Emery, *Science* **275**, 1102 (1997).
3. T. W. Ebbesen, H. J. Lezec, H. F. Ghaemi, T. Thio, P. A. Wolff, *Nature* **391**, 667 (1998).
4. W. L. Barnes, W. A. Murray, J. Dintinger, E. Devaux, T. W. Ebbesen, *Phys. Rev. Lett.* **92**, 107401 (2004).
5. R. W. Gruhlke, W. R. Holland, D. G. Hall, *Phys. Rev. Lett.* **56**, 2838 (1986).
6. D. K. Gifford, D. G. Hall, *Appl. Phys. Lett.* **81**, 4315 (2002).
7. S. Wedge, J. A. E. Wasey, I. Sage, W. L. Barnes, *Appl. Phys. Lett.* **85**, 182 (2004).
8. R. Charbonneau, P. Berini, E. Berolo, E. Lisicka-Shrzek, *Opt. Lett.* **25**, 844 (2000).
9. J. C. Weeber *et al.*, *Phys. Rev. B* **64**, 045411 (2001).
10. H. Ditlbacher, J. R. Krenn, G. Schider, A. Leitner, F. R. Aussenegg, *Appl. Phys. Lett.* **81**, 1762 (2002).
11. S. I. Bozhevolnyi, V. S. Volkov, *Opt. Lett.* **26**, 734 (2001).
12. W. L. Barnes, A. Dereux, T. W. Ebbesen, *Nature* **424**, 824 (2003).
13. J. R. Oppenheimer, *Phys. Rev.* **60**, 158 (1941).
14. M. Meier *et al.*, *Appl. Phys. Lett.* **74**, 7 (1999).
15. D. Dexter, *J. Chem. Phys.* **21**, 836 (1953).
16. T. Förster, *Annalen der Physik* **2**, 55 (1948).
17. T. Förster, *Discuss. Faraday Soc.* **27**, 7 (1959).
18. C. E. Finlayson, D. S. Ginger, N. C. Greenham, *Chem. Phys. Lett.* **338**, 83 (2001).
19. M. Hopmeier, W. Guss, M. Deussen, E. O. Göbel, R. F. Mahrt, *Phys. Rev. Lett.* **82**, 4118 (1999).
20. P. Andrew, W. L. Barnes, *Science* **290**, 785 (2000).
21. W. H. Weber, C. F. Eagen, *Opt. Lett.* **4**, 236 (1979).
22. D. Sarid, *Phys. Rev. Lett.* **47**, 1927 (1981).
23. J. B. Harris, T. W. Preist, J. R. Sambles, *J. Opt. Soc. Am. A* **12**, 1965 (1995).
24. G. W. Ford, W. H. Weber, *Phys. Rep.* **113**, 195 (1984).
25. W. L. Barnes, *J. Mod. Opt.* **45**, 661 (1998).
26. M. G. Salt, W. L. Barnes, *Opt. Commun.* **166**, 151 (1999).
27. P. Andrew, W. L. Barnes, data not shown.
28. We thank M. J. Jory for the R6G absorption spectrum data presented in Fig. 1D and the UK EPSRC and the EC (under project FP6 NMP4-CT-2003-505699) for financial support.

Enhancement of Ferroelectricity in Strained BaTiO₃ Thin Films

K. J. Choi,[1] M. Biegalski,[2] Y. L. Li,[2] A. Sharan,[2] J. Schubert,[3] R. Uecker,[4] P. Reiche,[4] Y. B. Chen,[5] X. Q. Pan,[5] V. Gopalan,[2] L.-Q. Chen,[2] D. G. Schlom,[2] C. B. Eom[1]*

Biaxial compressive strain has been used to markedly enhance the ferroelectric properties of BaTiO₃ thin films. This strain, imposed by coherent epitaxy, can result in a ferroelectric transition temperature nearly 500°C higher and a remanent polarization at least 250% higher than bulk BaTiO₃ single crystals. This work demonstrates a route to a lead-free ferroelectric for nonvolatile memories and electro-optic devices.

Enormous strains can exist in thin films when one material is deposited on another (1), resulting from differences in crystal lattice parameters and thermal expansion behavior between the film and the underlying substrate or arising from defects formed during film deposition (2, 3). As a result, the properties of thin films can be markedly different than the intrinsic properties of the corresponding unstrained bulk materials (4–9).

Although such strain often leads to degraded film properties, if judicious use is made of substrates and growth parameters, strain offers the opportunity to enhance particular properties of a chosen material in thin film form, namely strain engineering.

Strain engineering could facilitate the introduction of more environmentally benign ferroelectric random-access memories (FeRAM). Large shifts in the paraelectric-to-

[1]Department of Materials Science and Engineering, University of Wisconsin–Madison, Madison, WI 53706, USA. [2]Department of Materials Science and Engineering, Pennsylvania State University, University Park, PA 16802, USA. [3]Institut für Schichten und Grenzflächen ISG1-IT, Forschungszentrum Jülich GmbH, D-52425 Jülich, Germany. [4]Institute for Crystal Growth, Max-Born-Straße 2, D-12489 Berlin, Germany. [5]Department of Materials Science and Engineering, The University of Michigan, Ann Arbor, MI 48109, USA.

*To whom correspondence should be addressed. E-mail: eom@engr.wisc.edu

ferroelectric transition temperature (T_c) and remanent polarization (P_r) are expected (10–14) and have been observed (15–17) in ferroelectrics, signaling the viability of a strain-engineered advance for FeRAM. The major disadvantages of the two materials most widely being pursued for FeRAM (18), Pb(Zr,Ti)O$_3$ and SrBi$_2$Ta$_2$O$_9$, are (i) the volatility of the lead and bismuth constituents of these materials, which complicates their introduction into semiconductor fabrication facilities, and (ii) environmental issues associated with the toxicity of lead. We demonstrate that the ferroelectric properties of BaTiO$_3$ can be enhanced with the use of strain to make them viable for ferroelectric memory applications. The widespread use of (Ba,Sr)TiO$_3$ in semiconductor fabrication facilities for dynamic random-access memories (DRAM) greatly simplifies the introduction of this related material into silicon-based devices.

To predict the T_c enhancement and the temperature dependence of the lattice parameters of BaTiO$_3$ thin films under large biaxial strains with the use of Landau thermodynamic theories (10), we determined a new set of phenomenological coefficients, because existing ones are only applicable to small compressive strains (<~0.4%) (11). Figure 1 shows the T_c enhancement predicted from thermodynamic analysis for a BaTiO$_3$ thin film under biaxial strain $\varepsilon_s = (a_\parallel - a_0)/a_0$, where a_0 is the lattice parameter of free-standing cubic BaTiO$_3$ and $a_\parallel$ is the in-plane lattice parameter of a biaxially strained (001) BaTiO$_3$ film. The green region shows the range in predicted T_c resulting from the range of reported property coefficients for BaTiO$_3$ that enter into the thermodynamic analysis (19–21). Figure 1 implies that a biaxial compressive strain of only ~1% should be sufficient to produce strained (001) BaTiO$_3$ films with a T_c comparable to or higher than unstrained Pb(Zr,Ti)O$_3$ films.

Although Fig. 1 might seem to imply that T_c can be enhanced without bound, there are limits to strain engineering. The driving force for film relaxation increases with strain and film thickness. When films are grown to thicknesses greatly exceeding their critical values, relaxation toward a zero-strain state by the introduction of dislocations begins. Thus, for strain engineering to be effective, it is important to grow films below, or at least close to, their critical thickness for relaxation. Because the critical thickness at which dislocations begin to form varies approximately inversely with lattice mismatch (1), lower mismatch is desired to allow the growth of strained BaTiO$_3$ films that are thick enough to allow their ferroelectric properties to be conveniently probed or used in devices. Notably, Fig. 1 only applies to thick strained ferroelectrics; as

ferroelectrics get thin (<~100 Å), their ferroelectric properties can be substantially diminished by finite-size effects (17, 22–24). Optimizing the trade-off between strain and film thickness depends on the particular application. For FeRAM, films several hundred angstroms in thickness are needed (25). Based on the equilibrium critical thickness (1, 26) for BaTiO$_3$, this would constrain ε_s to be less than about 0.5%; however, we experimentally found that it is possible to grow coherent BaTiO$_3$ films at $\varepsilon_s = -1.7\%$ that are 500 Å thick.

We used the single-crystal substrates GdScO$_3$ and DyScO$_3$, because they are structurally (27), chemically (27), and thermally (28) compatible with BaTiO$_3$, and they have appropriate lattice constants to impart ε_s of about –1.0 and –1.7%, respectively, on coherent (001) BaTiO$_3$ films (21). Epitaxial BaTiO$_3$ thin films were grown on (110) GdScO$_3$ and (110) DyScO$_3$ substrates by reactive molecular beam epitaxy (MBE) and by pulsed-laser deposition (PLD) with in situ high-pressure reflection high-energy electron diffraction (21).

The lattice parameters of the strained (001) BaTiO$_3$ thin films are summarized in Table 1. These films are epitaxial, purely c-axis oriented (the c axis of all BaTiO$_3$ domains is perpendicular to the wafer surface), and, with the exception of the BaTiO$_3$ film on DyScO$_3$ that is 2000 Å thick, are

fully coherent with the substrates, without any resolvable lattice relaxation.

To identify the ferroelectric phase transition, the temperature dependence of the in-plane and out-of-plane lattice parameters of the films and substrates was measured with a variable-temperature four-circle x-ray diffractometer equipped with a two-dimensional (2D) area detector with an angular resolution of ~0.02°. Unstrained BaTiO$_3$ undergoes a ferroelectric transition at about 130°C from the high-temperature cubic phase ($Pm\bar{3}m$) to the low-temperature tetragonal phase ($P4mm$) (20). Figure 2A shows 2D images of the 002 and 202 diffraction peaks at selected temperatures from a BaTiO$_3$ single crystal as well as from coherent BaTiO$_3$ thin films grown on (110) GdScO$_3$ and (110) DyScO$_3$ substrates. There is no substantial change in the diffraction peaks of the BaTiO$_3$ thin films that are at or above $T_c \sim 130$°C. As expected, the single diffraction spot of the BaTiO$_3$ single crystal splits into two below 130°C, corresponding to a and c domains of the tetragonal ($P4mm$) ferroelectric phase.

The in-plane and out-of-plane lattice parameters of the strained BaTiO$_3$ films grown by MBE were determined from the 202 and 002 diffraction peaks and are plotted as a function of temperature in Fig. 2B. The in-plane lattice parameters of the BaTiO$_3$ are coherent to the underlying substrates over the entire temperature range (25° to 700°C). There are marked differences in the evolution of the lattice parameters with temperature between the unstrained BaTiO$_3$ single crystal and the strained BaTiO$_3$ thin films. Notably, the BaTiO$_3$ thin films never become cubic; they remain tetragonal as a re-
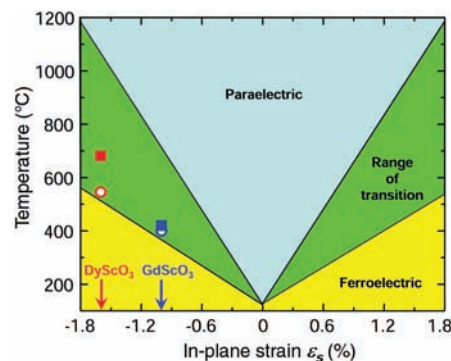
Table 1. Results from high-resolution x-ray diffraction measurements on the films. The in-plane (a) and out-of-plane (c) lattice constants and full width at half maximum (FWHM) of rocking curves of various peaks (002 of BaTiO$_3$, 200$_{pseudo-cubic}$ of SrRuO$_3$, and 200$_{pseudo-cubic}$ of GdScO$_3$ and DyScO$_3$) at room temperature are given. The a- and c-lattice parameters of single-crystalline BaTiO$_3$ are 3.992 and 4.036 Å, respectively (20).

	a (±0.002) (Å)	c (±0.0005) (Å)	FWHM (°)
Molecular beam epitaxy			
BaTiO$_3$ (1000 Å) on GdScO$_3$			
BaTiO$_3$	3.964	4.0693	0.080
GdScO$_3$	3.965	3.9638	0.009
BaTiO$_3$ (500 Å) on DyScO$_3$			
BaTiO$_3$	3.940	4.0953	0.120
DyScO$_3$	3.943	3.9396	0.009
Pulsed-laser deposition			
BaTiO$_3$ (2000 Å) on SrRuO$_3$ (1000 Å) on GdScO$_3$			
BaTiO$_3$	3.965	4.0692	0.042
SrRuO$_3$	3.968	3.9052	0.036
GdScO$_3$	3.964	3.9646	0.008
BaTiO$_3$ (500 Å) on SrRuO$_3$ (2000 Å) on DyScO$_3$			
BaTiO$_3$	3.939	4.0989	0.045
SrRuO$_3$	3.943	3.9110	0.022
DyScO$_3$	3.944	3.9396	0.009
BaTiO$_3$ (2000 Å) on SrRuO$_3$ (1000 Å) on DyScO$_3$			
BaTiO$_3$	3.958	4.0819	0.135
SrRuO$_3$	3.947	3.9187	0.047
DyScO$_3$	3.944	3.9398	0.009

Fig. 1. Expected T_c of (001) BaTiO$_3$ under biaxial in-plane strain (ε_s), based on thermodynamic analysis (10, 21). The green region represents the range (error bars) in the predicted T_c resulting from the spread in reported property coefficients (20, 21) for BaTiO$_3$ that enter into the thermodynamic analysis. The data points show the observed ε_s and T_c values of coherent BaTiO$_3$ films grown by MBE on GdScO$_3$ (blue circle) and DyScO$_3$ (red circle) substrates and by PLD on GdScO$_3$ (blue square) and DyScO$_3$ (red square) substrates.

sult of the biaxial substrate constraint. The predicted dependence of the *c*-lattice parameter of biaxially strained BaTiO$_3$, with and without a ferroelectric phase transition, was calculated from thermodynamic analysis (*10*) and is shown by the green solid and dashed curves in Fig. 2B, respectively. Because the BaTiO$_3$ film is clamped in-plane, all structural changes resulting from the phase transition and thermal expansion are accommodated through changes in the out-of-plane lattice parameter only. The agreement between the solid green prediction and the measured *c*-axis lattice parameters in Fig. 2B is strong evidence that the change in slope in the *c*-axis lattice parameter at high temperature corresponds to a ferroelectric phase transition. Analogous lattice constant behavior has been observed in other constrained ferroelectric films (*15*, *17*), is consistent with theory (*13*, *17*), and has been used to determine T_c. The T_c of the coherent BaTiO$_3$ thin films shown in Fig. 2B is ~400°C on GdScO$_3$ and ~540°C on DyScO$_3$.

To confirm the huge shifts in T_c, we attempted to measure polarization hysteresis loops on a 2000-Å-thick coherent BaTiO$_3$ film grown by PLD on a coherent SrRuO$_3$ bottom electrode on (110) GdScO$_3$. At temperatures up to about 200°C, hysteresis loops were clearly seen, but at higher temperatures the dielectric losses in the films became too high for reliable measurements. We made

second harmonic generation (SHG) measurements as a function of temperature on this PLD-grown BaTiO$_3$/SrRuO$_3$/GdScO$_3$ sample as well as the MBE-grown BaTiO$_3$/GdScO$_3$ sample, whose lattice constants versus temperature behavior is shown in Fig. 2B (*21*). An SHG signal is only exhibited by materials that lack inversion symmetry. All ferroelectrics must lack inversion symmetry, but there are many materials that lack inversion symmetry and are not ferroelectric. This makes SHG a necessary but insufficient probe for ferroelectricity. Nonetheless, SHG (Fig. 2C) shows that the phase we know from hysteresis loops to be ferroelectric at room temperature remains noncentrosymmetric to the same high temperature (*29*, *30*) at which x-ray diffraction indicates a phase transition. The interpretation consistent with all our analyses—x-ray diffraction, SHG, and hysteresis measurements—is that biaxial compressive strain increases the T_c of BaTiO$_3$.

Hysteresis measurements were made on 200-μm-diameter capacitors of strained BaTiO$_3$ thin films sandwiched between epitaxial top and bottom electrodes of the conducting perovskite oxide SrRuO$_3$ (*31*). High-resolution x-ray diffraction measurements (summarized in Table 1) revealed the BaTiO$_3$ ferroelectric layers as well as the 1000-Å-thick SrRuO$_3$ bottom electrodes to be fully coherent with the underlying substrates. No relaxation was observed even for

BaTiO$_3$ films as thick as 500 Å on DyScO$_3$ and 2000 Å on GdScO$_3$. The critical thicknesses of BaTiO$_3$ thin films grown on coherent SrRuO$_3$ bottom electrodes on GdScO$_3$ and DyScO$_3$ are higher than those of BaTiO$_3$ films grown directly on GdScO$_3$ and DyScO$_3$. This observation is consistent with critical thickness theory, in which the difference arises from strain partitioning between the layers as well as the altered geometry of misfit dislocations in a single layer versus a bilayer (*26*). Because the leakage in the coherent stack containing a 500-Å-thick BaTiO$_3$ layer on DyScO$_3$ was too high for good ferroelectric hysteresis measurements, a SrRuO$_3$/BaTiO$_3$/SrRuO$_3$/DyScO$_3$ stack was grown with a 2000-Å-thick BaTiO$_3$ layer. This latter stack had low leakage; however, it was partially relaxed.

Figure 3A shows the ferroelectric hysteresis loops measured on the ferroelectric stacks grown on GdScO$_3$ and DyScO$_3$ substrates with 2000-Å-thick BaTiO$_3$ layers, together with results from a BaTiO$_3$ single crystal (*32*). The hysteresis loops are shifted in the positive voltage direction. This imprint effect is probably due to the asymmetric interfacial properties of the top and bottom electrodes to the BaTiO$_3$ films. Even though we used SrRuO$_3$ for both electrodes, the growth temperature (350°C) of the top electrode was much lower than that of the bottom electrode (680°C), which might lead to poor crystallinity of the top electrode and

Fig. 2. (**A**) 2D images at selected temperatures of the x-ray diffraction peaks from a BaTiO$_3$ single crystal and strained BaTiO$_3$ thin films. (**B**) Temperature dependence of the lattice parameters of single-crystal BaTiO$_3$, and strained BaTiO$_3$ thin films grown by MBE on DyScO$_3$ substrates and GdScO$_3$ substrates. The in-plane (//) and out-of-plane ($\perp$) lattice constants of the BaTiO$_3$ thin films and underlying substrates are shown. The change in slope at high temperature
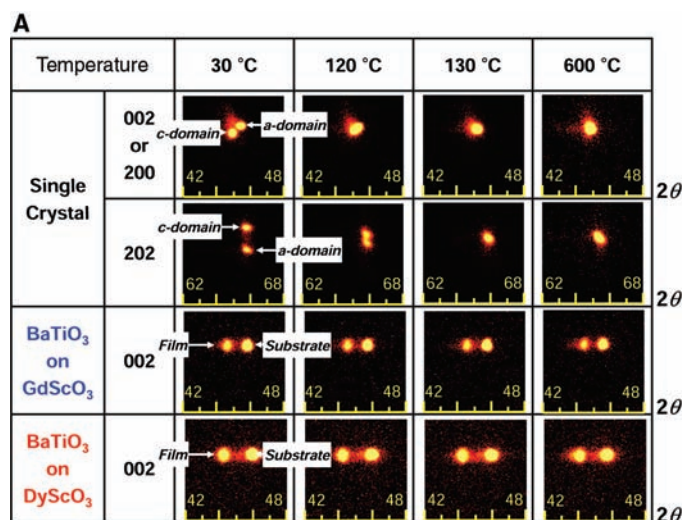
signals a phase transition. The error bars ($\pm$SD) of the measured lattice constants are shown to the left of each curve. The measured values of the out-of-plane lattice constant of biaxially strained BaTiO$_3$ are compared with theoretical predictions (*10*, *21*) with and without a ferroelectric transition. (**C**) Optical SHG signals from a BaTiO$_3$ single crystal [heating (black open circles) and cooling (black filled circles)] and the same strained BaTiO$_3$ on GdScO$_3$ film as (B) [heating (blue open squares) and cooling (blue filled squares)]. The fundamental wave (wavelength 900 nm, 65-fs laser pulses) is incident on the sample at an angle of $\varphi = 23°$ on the substrate side of the thin film and at normal incidence ($\varphi = 0°$) for the BaTiO$_3$ single crystal. SHG signals of 1 arbitrary unit (a.u.) or lower are at the noise level of our lockin-based measurement system. The inset shows polar plots of SHG intensity (radius) versus fundamental polarization (azimuth). Circles are experiment and solid lines are theory (*21*, *35*).
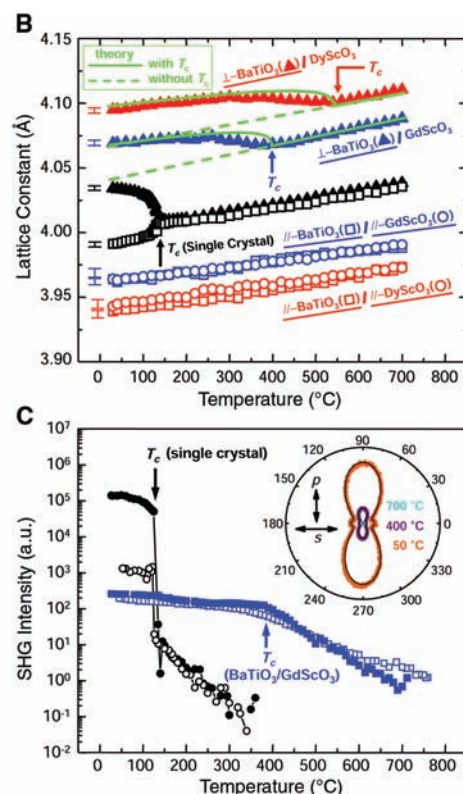
asymmetric interfaces. The P_r and coercive field (E_r) were determined to be ~50 μC/cm² and 80 kV/cm for the fully coherent BaTiO₃/GdScO₃ sample and ~70 μC/cm² and 25 kV/cm for the partially relaxed BaTiO₃/DyScO₃ sample, respectively. This P_r value is almost 270% of the 26 μC/cm² (32) of single crystal BaTiO₃, 3.5 times higher than the maximum switching charge density (20 μC/cm²) assumed in the scaling analysis of FeRAM (18), and comparable to the P_r of unstrained Pb(Zr,Ti)O₃ films (33). As this P_r of ~70 μC/cm² was observed in a partially relaxed sample with ε_s of –1.3%, a coherently strained BaTiO₃/DyScO₃ sample with ε_s of –1.7% could have an even higher P_r.

Another important issue for the application of ferroelectric capacitors to memory devices is the loss of switched polarization after repeated switching, i.e., fatigue. We performed fatigue measurements by applying 8.6-μs-wide pulses with a repetition frequency of 10 kHz to the top and bottom SrRuO₃ electrodes of the SrRuO₃/BaTiO₃/SrRuO₃/GdScO₃ structure at V_{max} = 4 V, where V_{max} is the amplitude of the voltage pulse. V_{max} = 4 V corresponds to 200 kV/cm of the electric field. The switched polarization decreased by 10% of its original value after 10⁶ fatigue cycles, but recovered its original value after 10¹⁰ cycles. This is consistent with previous observations of fatigue-free behavior when conducting oxide electrodes are used (34, 35).

As a check that the enhancement of T_c observed in coherently strained BaTiO₃ thin films grown by MBE (Fig. 2B) is inherent and applicable to a device structure with a conductive bottom electrode, we performed high-temperature x-ray diffraction measurements on the coherent BaTiO₃ thin films with SrRuO₃ bottom electrodes grown by PLD. Figure 3B shows the evolution of the in-plane (*a*) and out-of-plane (*c*) lattice parameters of the BaTiO₃ film and the GdScO₃ and DyScO₃ substrates as a function of temperature. The in-plane lattice parameters reveal that both the BaTiO₃ and SrRuO₃ layers are coherently strained to the underlying substrates over the entire temperature range. This is consistent with the absence of misfit dislocations along the interface between GdScO₃ and SrRuO₃ and along the interface between SrRuO₃ and BaTiO₃, as shown by the cross-sectional transmission electron microscope images in figs. S1 and S2 (21). As seen in the figure, the transition behavior of the PLD samples is quite similar to those grown by MBE. T_c was determined to be ~420° and ~680°C for samples grown on GdScO₃ and DyScO₃, respectively. The green solid and dashed lines in Fig. 3B are theoretical predictions of *c*-lattice parameters with and without the ferroelectric phase transition, which are fairly consistent with the experimentally measured values. The agreement in the results for films grown by MBE and PLD indicates that the observed shifts in ferroelectric properties with strain represent the intrinsic behavior of strained BaTiO₃. This experimental dependence of T_c on ε_s is also consistent with the expectations shown in Fig. 1.

In summary, we have demonstrated that the ferroelectric properties of BaTiO₃ can be markedly enhanced through strain engineering. These strain-engineered heteroepitaxial thin films provide a broad range of operating temperatures as well as higher remanent polarization for improved noise immunity and the ability to scale FeRAM to smaller cell sizes. Another application of strain-engineered BaTiO₃ films is high-speed electro-optic modulators, in which the sizeable electro-optic coefficients of BaTiO₃ can be enhanced by appropriate strain engineering. The ability to withstand huge strains gives thin films a degree of freedom absent from bulk. This can be exploited to enhance the ferroelectric properties of any ferroic system, including multiferroics (8, 22, 36), whose ferroic order parameter has a strong coupling to strain.

References and Notes
1. W. D. Nix, *Metall. Trans. A* **20**, 2217 (1989).
2. J. S. Speck, A. C. Daykin, A. Seifert, A. E. Romanov, W. Pompe, *J. Appl. Phys.* **78**, 1696 (1995).
3. W. D. Nix, B. M. Clemens, *J. Mater. Res.* **14**, 3467 (1999).
4. R. S. Beach et al., *Phys. Rev. Lett.* **70**, 3502 (1993).
5. H. Sato, M. Naito, *Physica C* **274**, 221 (1997).
6. Q. Gan, R. A. Rao, C. B. Eom, J. L. Garrett, M. Lee, *Appl. Phys. Lett.* **72**, 978 (1998).
7. I. Bozovic, G. Logvenov, I. Belca, B. Narimbetov, I. Sveklo, *Phys. Rev. Lett.* **89**, 107001 (2002).
8. J. Wang et al., *Science* **299**, 1719 (2003).
9. J. H. Haeni et al., *Nature* **430**, 758 (2004).
10. A. F. Devonshire, *Philos. Mag.* **42**, 1065 (1951).
11. N. A. Pertsev, A. G. Zembilgotov, A. K. Tagantsev, *Phys. Rev. Lett.* **80**, 1988 (1998).
12. Y. L. Li, S. Y. Hu, Z. K. Liu, L. Q. Chen, *Appl. Phys. Lett.* **78**, 3878 (2001).
13. M. Sepliarsky, S. R. Phillpot, M. G. Stachiotti, R. L. Migoni, *J. Appl. Phys.* **91**, 3165 (2002).
14. J. B. Neaton, K. M. Rabe, *Appl. Phys. Lett.* **82**, 1586 (2003).
15. E. D. Specht, H.-M. Christen, D. P. Norton, L. A. Boatner, *Phys. Rev. Lett.* **80**, 4317 (1998).
16. N. Yanase, K. Abe, N. Fukushima, T. Kawakubo, *Jpn. J. Appl. Phys.* **38**, 5305 (1999).
17. S. K. Streiffer et al., *Phys. Rev. Lett.* **89**, 067601 (2002).
18. The International Technology Roadmap for Semiconductors, *2003* (Semiconductor Industry Association, San Jose, CA, 2003), Front End Processes Section, pp. 50–56.
19. For biaxial tensile ($\varepsilon_s \geq 0$) or biaxial compressive ($\varepsilon_s \leq 0$) strains, T_c is expressed as follows: $T_c = \theta + 2\varepsilon_0 C \times \frac{Q_{11} + Q_{12}}{s_{11} + s_{12}}\varepsilon_s$ ($\varepsilon_s \geq 0$) or $T_c = \theta + 2\varepsilon_0 C \frac{2Q_{12}}{s_{11} + s_{12}}\varepsilon_s$ ($\varepsilon_s \leq 0$). In the equations, θ is the Curie-Weiss temperature of unstrained BaTiO₃, ε_0 is the permittivity of free space, C is the Curie constant, Q_{11} and Q_{12} are electrostrictive coefficients, and s_{11} and s_{12} are elastic compliances. The breadth of the green region in Fig. 1 for T_c is due to the variation in what are considered the most accurate reported values of these constants for BaTiO₃ single crystals (20, 21). Because $(Q_{11} + Q_{12}) > 0$ and $Q_{12} < 0$, T_c is predicted to increase for both positive and negative strains.
20. K.-H. Hellwege, A. M. Hellwege, Eds., *Landolt-Börnstein: Numerical Data and Functional Relationships in Science and Technology* (Springer, Berlin, 1981), New Series–Group III, vol. 16a, pp. 67, 73, 74.
21. Materials and methods are available as supporting material on *Science* Online.
22. C. H. Ahn, K. M. Rabe, J.-M. Triscone, *Science* **303**, 488 (2004).
23. J. Junquera, P. Ghosez, *Nature* **422**, 506 (2003).
24. D. D. Fong et al., *Science* **304**, 1650 (2004).
25. This thickness is a result of the low operational voltage of FeRAM [about 1.2 V in 2007 (18)] coupled with the need for a ferroelectric layer with low leakage. For reliable switching, the FeRAM operational voltage divided by the thickness of the ferroelectric should be several times larger than the coercive field of the ferroelectric. Thin film ferroelectrics have coercive fields of 10 to 100 kV/cm. This is true for our films as
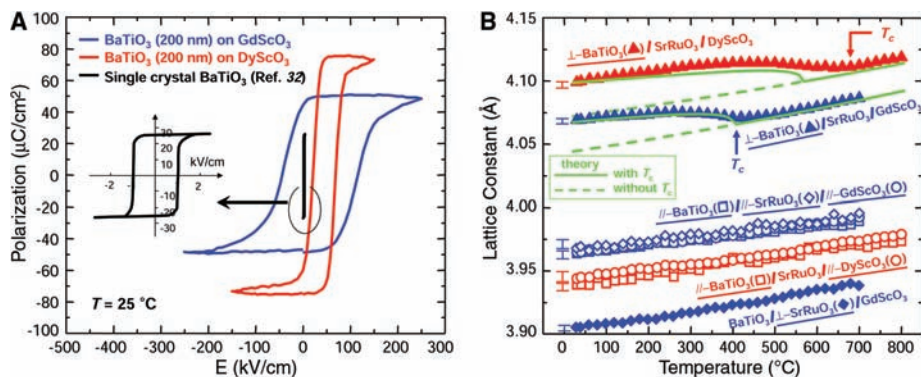

Fig. 3. (**A**) Polarization-electric field hysteresis loops of BaTiO₃ thin film capacitors (2000 Å) grown by PLD on GdScO₃ and DyScO₃ with SrRuO₃ top and bottom electrodes. The inset shows the hysteresis loop of an unstrained bulk BaTiO₃ single crystal for comparison (32). (**B**) Temperature dependence of the lattice parameters of strained SrRuO₃/BaTiO₃/SrRuO₃ capacitor structures grown by PLD on DyScO₃ substrates and GdScO₃ substrates. The in-plane (//) and out-of-plane (⊥) lattice constants of the BaTiO₃ thin films, SrRuO₃ bottom electrode, and underlying substrates are shown. The lattice parameters of the SrRuO₃ film on DyScO₃ could not be resolved because SrRuO₃ and DyScO₃ are isostructural with very similar lattice parameters. The change in slope at high temperature indicates a phase transition. The error bars (±SD) of the measured lattice constants are shown to the left of each curve. The measured values of the out-of-plane lattice constant of biaxially strained BaTiO₃ are compared with theoretical predictions (10, 21) with and without a ferroelectric transition.

well as the polycrystalline films used in today's FeRAM. This leads to an upper bound in film thickness of about 1000 Å. The thinness of the ferroelectric film is also constrained. First, there is an intrinsic finite-size effect in which the T_c begins to decrease at a thickness of about 100 Å (17, 22–24) and eventually vanishes for thicknesses in the 10 to 30 Å range (23, 24). The second reason is that extrinsic effects (pinholes and nonuniform thickness over the capacitor area) lead to unacceptably high leakage currents for FeRAM device operation.

26. J. W. Matthews, A. E. Blakeslee, *J. Cryst. Growth* **27**, 118 (1974).
27. J. Schubert *et al.*, *Appl. Phys. Lett.* **82**, 3460 (2003).
28. M. D. Biegalski *et al.*, unpublished data.
29. A small amount of symmetry-forbidden SHG signal is observed even above T_c in both the BaTiO$_3$ single crystal and thin films. This has been seen previously in single crystals, fibers, and powders of BaTiO$_3$ and is suggested to arise from metastable micropolar regions (compositional or physical defects) in the paraelectric phase of the crystal that locally break the inversion symmetry (30).
30. G. R. Fox, J. K. Yamamoto, D. V. Miller, L. E. Cross, S. K. Kurtz, *Mater. Lett.* **9**, 284 (1990).
31. C. B. Eom *et al.*, *Science* **258**, 1766 (1992).
32. B. Jaffe, W. R. Cook Jr., H. Jaffe, *Piezoelectric Ceramics* (Academic Press, London, 1971), p. 78.
33. V. Nagarajan *et al.*, *J. Appl. Phys.* **86**, 595 (1999).
34. R. Ramesh *et al.*, *Appl. Phys. Lett.* **61**, 1537 (1992).
35. C. B. Eom *et al.*, *Appl. Phys. Lett.* **63**, 2570 (1993).
36. A. Sharan *et al.*, *Phys. Rev. B* **69**, 214109 (2004).
37. We thank L. E. Cross, S. K. Streiffer, and S. Trolier-McKinstry for useful discussions. We also thank L. J. Belenky, D. M. Kim, and H. P. Sun for their help with the experiments. Supported by NSF through grants DMR-0313764, ECS-0210449, DMR-0103354, and DMR-0122638 and a David and Lucile Packard Fellowship (C.B.E.). K.J.C. acknowledges that this work was supported in part by the Postdoctoral Fellowship Program of Korea Science and Engineering Foundation (KOSEF).

Cation Exchange Reactions in Ionic Nanocrystals

Dong Hee Son,[1] Steven M. Hughes,[2] Yadong Yin,[1] A. Paul Alivisatos[1,2]*

Cation exchange has been investigated in a wide range of nanocrystals of varying composition, size, and shape. Complete and fully reversible exchange occurs, and the rates of the reactions are much faster than in bulk cation exchange processes. A critical size has been identified below which the shapes of complex nanocrystals evolve toward the equilibrium shape with lowest energy during the exchange reaction. Above the critical size, the anion sublattice remains intact and the basic shapes of the initial nanocrystals are retained throughout the cation exchange. The size-dependent shape change can also be used to infer features of the microscopic mechanism.

Chemical transformations from one solid to another via insertion and exchange of atoms can be used to modify the properties of crystalline materials (1). Recent developments have enabled the production of many technologically important crystalline materials in nanometer sizes, with a wide range of size- and shape-tunable properties (2–8). Of particular interest is the creation of nanocrystals with nonequilibrium shapes and with higher structural and compositional complexity (9–13). In extended solids, reactions involving chemical transformation are in general very slow because of high activation energies for the diffusion of atoms and ions in the solid. For this reason, typical solid-phase reactions require very high temperatures or pressures (14–16) and therefore would seem to be incompatible with kinetically controlled nonequilibrium nanostructures.

However, in crystals only a few nanometers in size, both the thermodynamics and kinetics of reactions can change with size. For example, a large surface-to-volume ratio can be accompanied by a lowering of phase transition temperatures (17, 18). With the decrease in the volume, statistical averaging of the kinetics and mechanisms over a distribution of heterogeneous reaction sites intrinsic to the bulk solid is also reduced, leading to more homogeneous molecule-like reaction kinetics and even different reaction mechanisms in nanocrystals (19). The optimal use of various chemical transformation methods to broaden the range of nanocrystalline materials depends on an understanding of how chemical transformations in a crystalline solid will be affected by a reduction in size. We show that cation exchange reactions can occur completely and reversibly in ionic nanocrystals at room temperature with unusually fast reaction rates. We also show that the crystal structure and morphology of the reaction products are strongly dependent on the size and shape of the nanocrystals.

The prototypical semiconductor nanocrystal system of CdSe reacts with Ag$^+$ ions to yield Ag$_2$Se nanocrystals by the forward cation exchange reaction, and vice versa for the reverse cation exchange reaction. We chose to work with CdSe nanocrystals because of the high degree of control over size and shape that has been achieved (2, 3). The conversion to Ag$_2$Se is strongly favored by a thermodynamic driving force of about –1000 kJ/mol in the bulk (20, 21). Ag$_2$Se also exhibits an interesting temperature-dependent polymorphism: The superionic conducting phase transition occurs at a relatively low temperature of 133°C in the bulk phase (22). Thus, it may be possible to prepare Ag$_2$Se with unusually high cation mobility. These two factors favor complete cation exchange in nanocrystals and may prove sufficient to overcome the fact that the exchange reaction is completely kinetically hindered at ambient temperature and pressure in the bulk.

We investigated the reaction by mixing a solution of CdSe nanocrystals (diameter 4.2 nm) in toluene with a small amount of methanolic solution of AgNO$_3$ under ambient conditions. The volume fraction of methanol in the solution mixture is about 1%; the solution contains Ag$^+$ ion in a slightly larger amount than necessary to replace all the Cd^{2+} ions in the nanocrystals. Methanol more strongly binds to any free binary cations in solution and thus favors the forward reaction. A rapid (≪1 s) change of solution color and complete disappearance of fluorescence is observed upon mixing the solutions. Measurements of the x-ray diffraction (XRD) patterns and optical absorption spectra confirm that the reaction product is Ag$_2$Se (Fig. 1). The reverse reaction is done under ambient conditions by mixing Ag$_2$Se nanocrystals with an excess amount (typically 50 to 100 times the initial Cd^{2+} content) of Cd(NO$_3$)$_2$ in a mixture of toluene and methanol in the presence of tributylphosphine (volume fraction <3%). A slower color change back to that of CdSe nanocrystals and the reappearance of fluorescence are observed over a period of 1 min. XRD patterns, optical absorption, and fluorescence spectra all indicate that CdSe is recovered from the reverse cation exchange. The XRD linewidths of the initial and recovered case are nearly identical. Moreover, the absorption and fluorescence peak positions, which show strong size dependence due to the quantum confinement effect (2), are also nearly identical for the initial and recovered CdSe nanocrystals. Finally, transmission electron micrograph (TEM) images of the initial and recovered

[1]Materials Sciences Division, Lawrence Berkeley National Laboratory, Berkeley, CA 94720, USA. [2]Department of Chemistry, University of California, Berkeley, CA 94720, USA.

*To whom correspondence should be addressed. E-mail: alivis@berkeley.edu

Thermodynamic Calculations

In a phenomenological description of the ferroelectric phase transitions in BaTiO₃, the spontaneous polarization $P = (P_1, P_2, P_3)$ is chosen as the order parameter. The Landau-Devonshire free energy, f, is usually expanded as a polynomial of the polarization components P_i $(i = 1,2,3)$. The order of the polynomial should be at least fourth-order for a second-order transition and sixth-order for a first-order transition (1, 2). In order to describe the three ferroelectric transitions in a BaTiO₃ single crystal, i.e., from paraelectric cubic to ferroelectric tetragonal, orthorhombic and rhombohedral, we expressed the Landau-Devonshire free energy with an eighth-order polynomial. Under stress-free conditions it is

$$
\begin{aligned}
f = {} & \alpha_1\left(P_1^2 + P_2^2 + P_3^2\right) + \alpha_{11}\left(P_1^4 + P_2^4 + P_3^4\right) + \alpha_{12}\left(P_1^2 P_2^2 + P_2^2 P_3^2 + P_1^2 P_3^2\right) \\
& + \alpha_{111}\left(P_1^6 + P_2^6 + P_3^6\right) + \alpha_{112}\left[P_1^2\left(P_2^4 + P_3^4\right) + P_2^2\left(P_1^4 + P_3^4\right) + P_3^2\left(P_1^4 + P_2^4\right)\right] \\
& + \alpha_{123} P_1^2 P_2^2 P_3^2 \\
& + \alpha_{1111}\left(P_1^8 + P_2^8 + P_3^8\right) + \alpha_{1112}\left[P_1^6\left(P_2^2 + P_3^2\right) + P_2^6\left(P_1^2 + P_3^2\right) + P_3^6\left(P_1^2 + P_2^2\right)\right] \\
& + \alpha_{1122}\left(P_1^4 P_2^4 + P_2^4 P_3^4 + P_1^4 P_3^4\right) + \alpha_{1123}\left(P_1^4 P_2^2 P_3^2 + P_2^4 P_3^2 P_1^2 + P_3^4 P_1^2 P_2^2\right),
\end{aligned}
\tag{1}
$$

where all of the coefficients are assumed to be temperature-independent except $\alpha_1 = (T - \theta)/(2\varepsilon_0 C) = \alpha_0(T - \theta)$, ε_0 is the permittivity of vacuum, C is the Curie-Weiss constant, and θ is the Curie-Weiss temperature.

The free energy of a tetragonal c-domain with $P = (0,0,P_3)$ in a BaTiO₃ film as a function of biaxial compressive strain, ε_s, is given by (3)

$$
f_T^{film} = \left(\alpha_1 + \beta_3\right)P_3^2 + \left(\alpha_{11} + \beta_{33}\right)P_3^4 + \alpha_{111}P_3^6 + \alpha_{1111}P_3^8 + \frac{\varepsilon_s^2}{s_{11} + s_{12}},
\tag{2}
$$

with $\beta_3 = -\dfrac{2Q_{12}\varepsilon_s}{s_{11} + s_{12}}$ and $\beta_{33} = \dfrac{Q_{12}^2}{s_{11} + s_{12}}$, where Q_{11} and Q_{12} are the electrostrictive coefficients and

s_{11} and s_{12} are elastic compliances. The spontaneous polarization of a tetragonal c-domain as a

function of temperature can be obtained by minimizing the free energy, Eq. (2), with respect to

P_3.

When the transition from paraelectric to tetragonal is second-order, the transition

temperature can be obtained through $\alpha_1 + \beta_3 = 0$, i.e.,

$$T_c = \theta + 2\varepsilon_0 C \frac{2Q_{12}}{s_{11} + s_{12}} \varepsilon_s. \tag{3}$$

If the transition is first-order, the transition temperature will be larger than that given by Eq. (3),

but the difference will be less than 10 °C, since it is a weak first-order transition (1). The

calculated transition temperature of the films as a function of strain (Fig. 1) has a range due to the

discrepancy among the reported data for the relevant coefficients for single crystal BaTiO$_3$ (1,

4-7), i.e., $Q_{11} = (0.100 \text{ to } 0.113) \text{ m}^4/\text{C}^2$, $Q_{12} = (-0.050 \text{ to } -0.034) \text{ m}^4/\text{C}^2$,

$C = (1.37 \text{ to } 1.73) \times 10^5 \text{ °C}$, $s_{11} + s_{12} = (5.2 \text{ to } 6.4) \times 10^{-12} \text{ m}^2/\text{N}$, and $\theta = (110 \text{ to } 118) \text{ °C}$.

By taking into account the stress-free surface condition and the biaxial substrate constraint,

the out-of-plane lattice parameter, c, as a function of temperature can be calculated from

$$c = a_c \left\{ 1 + \left[\frac{2s_{12}\varepsilon_s}{s_{11} + s_{12}} + P_3^2 \left(Q_{11} - \frac{2s_{12}Q_{12}}{s_{11} + s_{12}} \right) \right] \right\}, \tag{4}$$

where a_c is the lattice constant of stress-free bulk cubic BaTiO$_3$. In calculating c from Eq. (4) for

Figs. 2B and 3B, specific values of the relevant coefficients are used so the shape of the curve is

not obscured by the range of coefficient values. The following coefficients are used:

$Q_{11} = 0.10 \text{ m}^4/\text{C}^2$, $Q_{12} = -0.034 \text{ m}^4/\text{C}^2$ (4); $s_{11} = 9.1 \times 10^{-12} \text{ m}^2/\text{N}$, $s_{12} = -3.2 \times 10^{-12} \text{ m}^2/\text{N}$ (7, 8);

$C_0 = 1.37 \times 10^5$ (from the dielectric constant measurements we made on the same BaTiO$_3$ single crystal whose lattice parameters as a function of temperature are shown in Fig. 2A); $\theta = 115°C$ (9); $\alpha_{11} = -508.55\,\alpha_0\ \mathrm{N\,m^6/C^4}$, $\alpha_{111} = 3137.11\,\alpha_0\ \mathrm{N\,m^{10}/C^6}$; $\alpha_{1111} = 93673.45\,\alpha_0\ \mathrm{N\,m^{14}/C^8}$. These values are from our new fitting of the data for BaTiO$_3$ single crystals under stress-free conditions, yielding $P_c = 18.12\ \mu C/cm^2$ at the transition temperature $T_c = 125°C$, $P_s = 26\ \mu C/cm^2$ at $T = 25°C$ and $P_s = 23\ \mu C/cm^2$ at $T = 87°C$. The details of the determination of these coefficients will be reported in a follow-up paper (10). Considering the experimental results in Figs. 1, 2B, and 3B, these coefficients seem to be well suited to the BaTiO$_3$ films grown by both MBE and PLD in this study.

Substrates

The (110) GdScO$_3$ and (110) DyScO$_3$ substrates used are two of a series of rare-earth scandates with pseudocubic lattice constants that range from to 3.93 Å to 4.05 Å in roughly 0.01 Å increments as the rare earth species is varied (11-17). These rare earth scandates have the GdFeO$_3$-type orthorhombic structure (space group: *Pbnm*). GdScO$_3$ has lattice constants $a = 5.488$ Å, $b = 5.746$ Å, and $c = 7.934$ Å (14) and DyScO$_3$ has lattice constants $a = 5.440$ Å, $b = 5.713$ Å, and $c = 7.887$ Å (15). In these structures the (110) plane, spanned by $[1\bar{1}0]$ and [001] directions, provides a nearly square base with $c/2 = 3.967$ Å and $\sqrt{a^2+b^2}/2 = 3.973$ Å for the in-plane surface mesh of (110) GdScO$_3$ (14, 17) and $c/2 = 3.943$ Å and $\sqrt{a^2+b^2}/2 = 3.944$ Å for (110) DyScO$_3$ (15, 17). Thus, (110) GdScO$_3$ and (110) DyScO$_3$ substrates provide ε_s of about -1.0% and -1.7%, respectively, for the epitaxial growth of coherent (001) BaTiO$_3$ films.

Thin Film Growth

Epitaxial BaTiO$_3$ thin films were grown on (110) GdScO$_3$ and (110) DyScO$_3$ substrates by both MBE and PLD. For the films grown by MBE, molecular beams of the constituent elements were supplied to the surface of untwinned (110) GdScO$_3$ and (110) DyScO$_3$ substrates held at 700 °C. A mixture of 90% O$_2$ and 10% ozone at a background pressure of 5×10^{-6} Torr was used as the oxidant, incident upon the substrate via a directed inlet nozzle. The BaTiO$_3$ was deposited by the sequential deposition of BaO and TiO$_2$ monolayers, where each monolayer dose was controlled in real time by feedback from reflection high-energy electron diffraction (RHEED) intensity oscillations (*18*). To grow BaTiO$_3$ films by PLD, untwined (110) GdScO$_3$ and (110) DyScO$_3$ substrates were attached to a resistive heater and positioned 5.0 cm from the target. A KrF excimer laser (248 nm) beam was focused on a stoichiometric BaTiO$_3$ target to an energy density of 2.0 J/cm^2 and pulsed at 5 Hz. BaTiO$_3$ films were grown at substrate temperatures ranging from 650 to 800 °C and oxygen pressures of 100-150 mTorr. The PLD system is equipped with high-pressure RHEED, which enabled the layer-by-layer growth of the thin films to be monitored in situ during growth.

Structural Characterization

The three-dimensional strain state of the films was determined using high-resolution four-circle x-ray diffraction. The crystalline perfection of the films was assessed by measuring the full width at half maximum (FWHM) in ω (rocking curve) of the 002 BaTiO$_3$ reflection.

The microstructure and interfacial structure of the BaTiO$_3$ thin films grown on both GdScO$_3$ and DyScO$_3$ substrates were characterized by cross-sectional transmission electron microscopy (TEM). Figure S1A is a bright-field TEM image showing a 200 nm thick BaTiO$_3$ film grown on a (110) GdScO$_3$ substrate with a (110) SrRuO$_3$ bottom electrode layer. The

corresponding selected area electron diffraction patterns for each film layer and the substrate are also shown in Fig. S1. It was found that the BaTiO$_3$ film grows epitaxially and is purely c-axis oriented normal to the substrate through the whole film. No misfit dislocations are seen along the interface between GdScO$_3$ and SrRuO$_3$ or along the interface between SrRuO$_3$ and BaTiO$_3$. This indicates that both the SrRuO$_3$ and BaTiO$_3$ films are strained to the lattice spacing of the substrate by coherent epitaxial growth, which is consistent with the x-ray data shown in Fig. 3B and Table 1. The change in the diffraction contrast of the BaTiO$_3$ film indicates that the film is highly strained. High-resolution TEM images of the BaTiO$_3$/SrRuO$_3$ and SrRuO$_3$/GdScO$_3$ interfaces are shown in Fig. S2. Sharp interfaces are seen both between GdScO$_3$ and SrRuO$_3$ and between SrRuO$_3$ and BaTiO$_3$. The position of the interfaces is indicated by dashed lines.
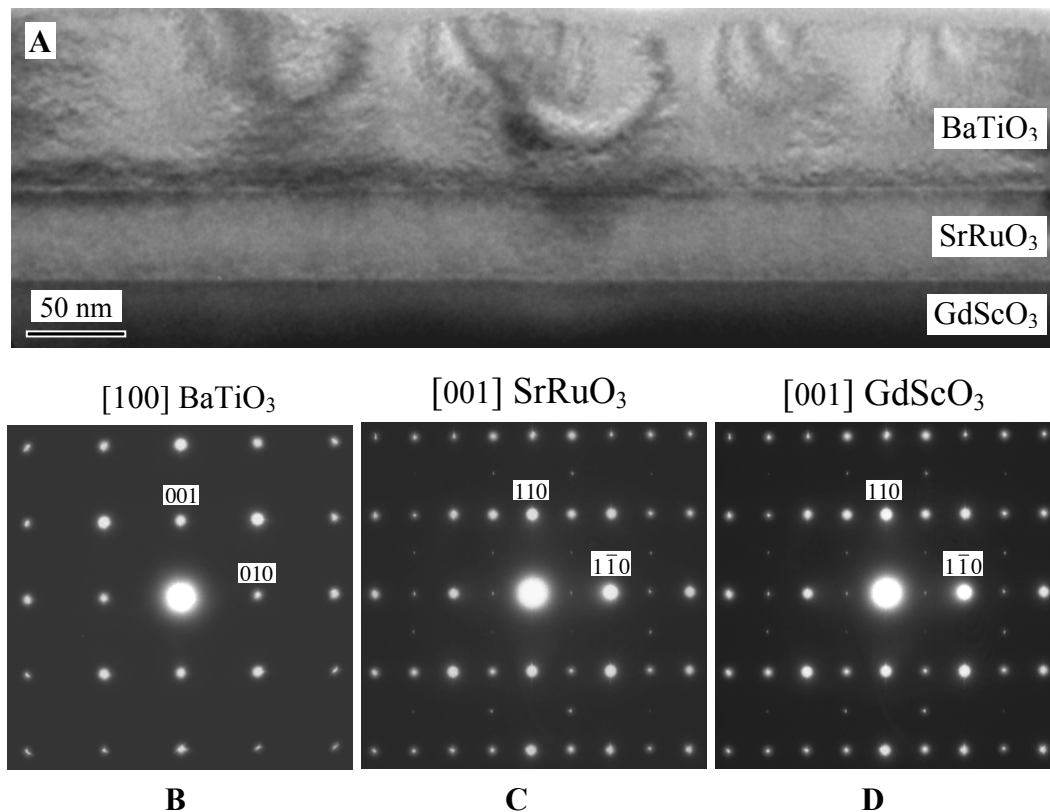

Fig. S1. (A) Bright-field TEM image showing a 200 nm thick BaTiO$_3$ film grown on a (110) GdScO$_3$ substrate with a (110) SrRuO$_3$ bottom electrode layer. (B), (C), and (D) Selected area electron diffraction patterns corresponding to the BaTiO$_3$ and SrRuO$_3$ films and the GdScO$_3$ substrate, respectively.
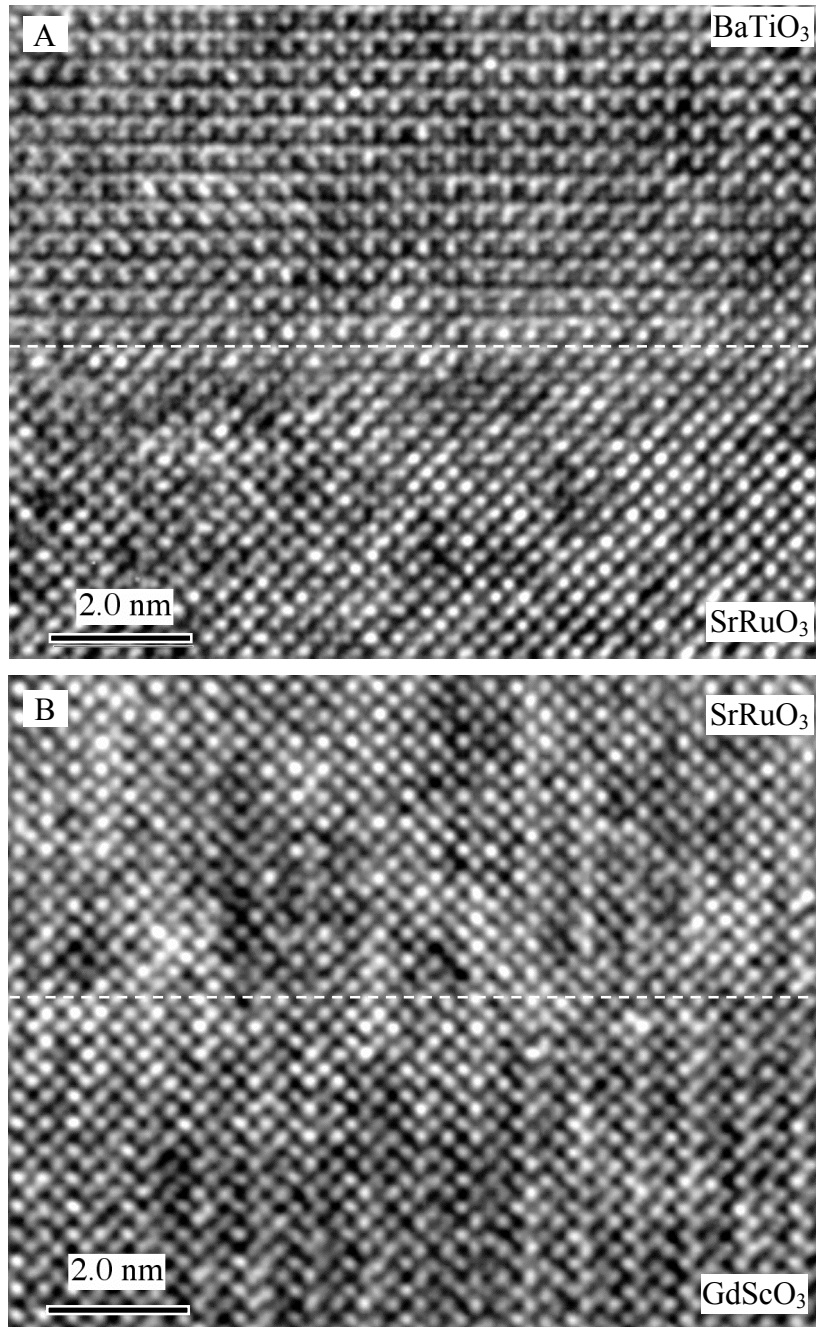
Fig. S2. High-resolution TEM images showing **(A)** the BaTiO$_3$/SrRuO$_3$ and **(B)** the SrRuO$_3$/GdScO$_3$ interfaces. Dashed lines mark the position of the interfaces.

Second Harmonic Generation Measurements

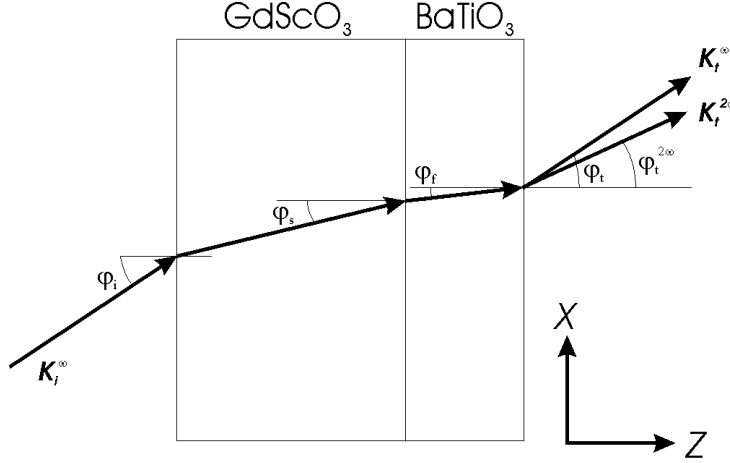A schematic of the SHG measurement is shown in Fig. S3.

Fig. S3. A schematic of the geometry of the SHG measurement (not to scale). The wavevectors k^{ω} and $k^{2\omega}$, for fundamental frequency (ω) and second harmonic frequency (2ω), are shown. The incidence and refraction angles φ, are also shown, with subscripts, *i, s, f,* and *t*, corresponding to *incidence, substrate, film,* and *transmitted,* respectively.

To measure the polar plots in the inset of Fig. 2C, incident light at frequency ω (wavelength 900 nm) was polarized at an angle of θ to the *x-y* plane and $\varphi_i = 23°$ to the surface normal (*z*) of the GdScO$_3$ substrate. The incident fundamental polarization was *p*-polarized and the output SHG polarization ($I^{2\omega}$ at frequency 2ω (wavelength of 450 nm)) was *p*-polarized ($\theta = 0°$) for the film and *s*-polarized ($\theta = 90°$) for the single crystal.

The general expression for this SHG intensity is given by (*19-21*)

$$I^{2\omega} = K_1\left(\cos^2\theta + K_2\sin^2\theta\right)^2 + K_3\sin^2(2\theta), \qquad (5)$$

where K_1, K_2, and K_3 are constants that depend on nonlinear coefficients (d_{31}, d_{33}, and d_{15}), geometric factors involving Fresnel coefficients, angles shown in Fig. S3, and microstructural parameters involving the relative area fraction of various polarization variants (domains) in the BaTiO$_3$ film. Detailed analysis of the derivation, and the physical significance of all the fitting parameters will be reported elsewhere.

No SHG signal was detected for normal incidence on the film system ($\varphi_i = 0°$) in Fig. 2C, confirming that the strained BaTiO$_3$ film is indeed predominantly c-axis (001) oriented. X-ray diffraction measurements revealed that following the temperature cycling of the SHG measurement shown in Fig. 2C, the film contained ~0.8% by volume of a-domains. These domains have polarization P_s along the $\pm x$ and $\pm y$ directions.

The first term in Eq. (5) involving the constants K_1 and K_2 arises predominantly from domains with polarization P_s along the $\pm z$ directions, and possibly a small amount of contribution from domains with P_s along the $\pm x$ directions. The second term arises from a small SHG contribution from domains with polarization P_s along the $\pm y$ directions. The ratio, $I^{2\omega}(\theta = 0°)/I^{2\omega}(\theta = 90°)=1/K_2^2$, corresponding to the ratio of p-to-s polarized SHG intensity from the film, is related purely to intrinsic nonlinear coefficients of the film (d_{31}, d_{33}, and d_{15}) and fixed geometric factors, and is independent of the film domain microstructure. Numerical fitting of the polar plots yields the constant $1/K_2 = -2.2 \pm 0.01$, which is therefore related to intrinsic BaTiO$_3$ material properties. This constant is found to remain constant between 50 °C and 400 °C in the polar plots, but decreases thereafter in polar plot measurements up to 700 °C. This indicates a discontinuity in the intrinsic material property beyond the T_c in the strained BaTiO$_3$ film.

References

S1. F. Jona, S. Shirane, *Ferroelectric Crystals* (Pergamon Press, Oxford, 1962).

S2. A. F. Devonshire, *Philos. Mag.* **40,** 1040 (1949).

S3. N. A. Pertsev, A. G. Zembilgotov, A. K. Tagantsev, *Phys. Rev. Lett.* **80,** 1988 (1998).

S4. T. Yamada, *J. Appl. Phys.* **43,** 328 (1972).

S5. K.-H. Hellwege, A. M. Hellwege, Eds., *Landolt-Börnstein: Numerical Data and Functional Relationships in Science and Technology* (Springer, Berlin, 1981), New Series, Group III, vol. 16a, pp. 67, 73, 74.

S6. K.-H. Hellwege, A. M. Hellwege, Eds., *Landolt-Bornstein: Numerical Data and Functional Relationships in Science and Technology* (Springer, Berlin, 1979), New Series, Group III, vol. 11, pp. 34, 418.

S7. A. F. Devonshire, *Philos. Mag.* **42,** 1065 (1951).

S8. D. Berlincourt, H. Jaffe, *Phys. Rev.* **111,** 143 (1958).

S9. S. H. Wemple, M. Didomenico, I. Camlibel, *J. Phys. Chem. Solids* **29** (1968).

S10. Y. L. Li *et al.*, unpublished.

S11. S. Geller, *Acta Cryst.* **10**, 243 (1957).

S12. J-M. Badie, *High Temp. High Pressures* **2**, 309 (1970).

S13. K.-H. Hellwege, A. M. Hellwege, Eds., *Landolt-Börnstein: Numerical Data and Functional Relationships in Science and Technology* (Springer, Berlin, 1976), New Series, Group III, vol. 7e, pp. 11-13.

S14. W.F. McClune, M.E. Mrose, B. Post, S. Weissmann, H.F. McMurdie, E. Evans, W. Wong-Ng, Eds., *Powder Diffraction File: Sets 27 to 28* (JCPDS International Centre for Diffraction Data, Swarthmore, 1986), p. 78. Card 27-220.

S15. W.F. McClune, M.E. Mrose, B. Post, S. Weissmann, H.F. McMurdie, E. Evans, W. Wong-Ng, Eds., *Powder Diffraction File: Sets 27 to 28* (JCPDS International Centre for Diffraction Data, Swarthmore, 1986), p. 72. Card 27-204.

S16. S. N. Amanyan, E. V. Antipov, V. A. Antonov, P. A. Arsen'ev, K. S. Bagdasarov, A. M. Kevorkov, L. M. Kovba, A. V. Rakhmatulin, *Russ. J. Inorg. Chem.* **32**, 1225 (1987).

S17. J. Schubert *et al.*, *Appl. Phys. Lett.* **82**, 3460 (2003).

S18. J. H. Haeni, C. D. Theis, D. G. Schlom, *J. Electroceram.* **4,** 385 (2000).

S19. Y. Barad *et al.*, *J. Appl. Phys.* **89**, 1387 (2001); **89**, 5230(E) (2001).

S20. Y. Barad, J. Lettieri, C. D. Theis, D. G. Schlom, V. Gopalan, *J. Appl. Phys.* **90**, 3497 (2001).

S21. A. Sharan *et al.*, *Phys. Rev. B* **69**, 214109 (2004).